RSC Advances

PAPER

View Article Online
View Journal | View Issue

Cite this: *RSC Adv.*, 2024, **14**, 34938

Durable fluorinated cobalt oxyhydroxide/calcium alginate hydrogels for activating peroxymonosulfate to enable nearly 100% degradation of ciprofloxacin†

Yunxiong Zeng,[a] Zhilong Zhang,[a] Xingyu Zhan,[a] Bo Hong,[a] Xinqing Wang [a] and Yingchun Xia *[bc]

Peroxymonosulfate (PMS) activation by solid catalysts for ciprofloxacin (CIP) removal is a promising method for decontaminating wastewater. However, mainstream catalysts suffer from efficiency and durability issues due to mechanical fragility and structural instability. Here, we have developed a durable calcium alginate hydrogel encapsulating fluorinated cobalt oxyhydroxide (FCO/CAH), fabricated by a simple hydrogen-bond-assisted cross-linking reaction, to enhance PMS activation for complete CIP removal. The optimized 2-FCO/CAH could generate abundant singlet oxygen ($^1O_2$) and sulfate radicals ($SO_4^{\bullet-}$) with PMS, resulting in 0.433 min^{-1} kinetic constant and approximately 100% CIP degradation within 10 minutes. This exceptional degradation efficiency is due to the even distribution of 2-FCO, which maximizes catalytic sites for PMS activation, and the multichannel cavity structure of CAH, which effectively enriches both PMS and CIP. Furthermore, the durability of 2-FCO/CAH was proved by its negligible decay in CIP removal efficiency (~100%) and good microstructure retention after 6 consecutive cycles, facilitated by a stable surface reconstructed interphase on the 2-FCO surface and the strong mechanical property of 2-FCO/CAH. Our work showcases a facile approach to constructing durable hydrogel catalysts that improve PMS-mediated antibiotic degradation.

Received 1st September 2024
Accepted 14th October 2024

DOI: 10.1039/d4ra06321j

rsc.li/rsc-advances

Introduction

The rise in the number of micropollutants in aquatic ecosystems poses a significant threat to environmental health and human safety, prompting an urgent need for effective remediation strategies.[1–3] Ciprofloxacin (CIP), a representative of these emerging contaminants, is found in water bodies at extremely low concentrations, making it challenging to treat using conventional methods.[4–6] Due to the high chemical stability of CIP, advanced oxidation processes (AOPs) are now considered a more effective alternative for decomposing such refractory compounds than conventional chemistry methods.[7,8] Among these processes, peroxymonosulfate (PMS)-based AOPs are becoming popular for their ability to generate highly reactive species, particularly the potent $SO_4^{\bullet-}$, which plays a crucial role in degrading CIP.[9,10]

The efficacy of AOPs depends on the catalysts' ability to activate PMS and generate reactive species, and developing catalysts is thus a key focus in advancing AOPs for antibiotic removal.[11–13] Among explored diverse catalysts (*e.g.*, carbonaceous materials, transitional metals, and derived compounds),[14–16] cobalt-based catalysts are highly efficient in activating PMS, leading to ongoing exploration of cobalt-containing materials. Cobalt-contained materials can efficiently decompose PMS to generate a plethora of active species, especially the long-lived and highly active $SO_4^{\bullet-}$ and singlet oxygen ($^1O_2$), which can rapidly and completely remove CIP. Therefore, the development of such cobalt-based materials is a hot topic among researchers. Ma *et al.*[17] unveiled the structure–activity relationship between cobalt species and PMS to generate $^1O_2$ for complete removal of pollutants. Zhang *et al.*[16] demonstrated that cobalt oxyhydroxide/activated carbon composites, synthesized through wet chemical sedimentation, could rapidly degrade CIP with PMS activation, outperforming individual components by significant margins.

Currently, these cobalt-included materials in form of powder, widely studied in the mainstream, face significant challenges such as aggregation and loss during recycling. Furthermore, their dissolution in water can lead to cobalt leaching, posing a risk of secondary contamination. These issues significantly hinder the ease of scaling up and operational efficiency, thereby limiting the

[a]*College of Materials and Chemistry, Zhejiang Province Key Laboratory of Magnetic Materials, China Jiliang University, Hangzhou 310018, People's Republic of China*
[b]*Department of Chemical Engineering, Tsinghua University, Beijing 100084, People's Republic of China. E-mail: xiayc6@163.com*
[c]*Hefei Institute for Public Safety Research, Tsinghua University, Hefei 230601, People's Republic of China*

† Electronic supplementary information (ESI) available. See DOI: https://doi.org/10.1039/d4ra06321j

extensive application of powdered cobalt-containing materials in sewage water purification in practical scenarios.[18–20] Membranoid materials and non-woven fabrics used for immobilizing powdery catalysts have been considered acceptable strategies to solve the drawbacks of powdery catalysts and prevent their secondary environmental pollution.[21–23] Zeng *et al.* used a polyvinylidene fluoride (PVDF) membrane to immobilize carbon nitride oxide nanorods, effectively degrading tetracycline while preventing catalyst leakage.[14] However, current membranoid catalysts generally compromise removal efficiency and material structural stability compared to powdered counterparts because of reduced contact with pollutants, enlarged mass transfer resistance, and inferior activity.[24] Very recently, Zhan *et al.*[24] successfully used calcium hydrogel to trap photo-responsive carbon nitride powders, achieving nearly complete CIP degradation within 12 minutes under visible light irradiation, a performance comparable to that of powdered nanocatalysts. This work provides new insights into designing highly efficient and robust hydrogel-based catalysts for activating PMS to remove CIP.

Herein, we synthesized a calcium alginate hydrogel encapsulating fluorinated cobalt oxyhydroxide (FCO/CAH) through collective hydrogen-bond-assisted cross-linking reactions among sodium alginate (SA), Ca^{2+}, and FCO (Scheme 1). The optimal formulation (*i.e.*, 2-FCO/CAH) exhibits approximately 100% degradation of CIP in the presence of 2 mM PMS. The superior removal efficiency is due to the enhanced activation of PMS facilitated by the unique multichannel cavity structure of CAH and the evenly distributed 2-FCO. The 2-FCO/CAH has good catalyst durability due to its strong mechanical properties and a compact, surface reconstructed interphase formed during cycling. We systematically determined degradation mechanisms, intermediates, and associated toxicities using high-performance liquid chromatography-mass spectra (HPLC-MS), electron paramagnetic resonance (EPR) and biological tests.

Experimental section

Chemicals

Ammonium fluoride ($NH_4 \cdot F$, 99.5%), cobalt nitrate hexahydrate ($Co(NO_3)_2 \cdot 6H_2O$, 99.5%), calcium chloride ($CaCl_2$, 99.9%), urea ($CO(NH_2)_2$, 99.5%), sodium alginate ($C_6H_7NaO_6$, 100 kDa, 90%), sodium chloride (NaCl, 99.5%), peroxymonosulfate (PMS, $KHSO_5 \cdot \frac{1}{2}KHSO_4 \cdot \frac{1}{2}K_2SO_4$), ciprofloxacin (CIP, $C_{17}H_{18}FN_3O_3$, 98%), L-histidine (L-his, 99%), isopropyl alcohol (IPA, ≥99.5%), methanol (MeOH, 99.5%), sodium carbonate (Na_2CO_3, 99.5%), sodium bicarbonate ($NaHCO_3$, 99.5%), benzoquinone (BQ, 97%), humic acid (HA, ≥90%), bovine serum albumin (BSA), 5,5-dimethyl-1-pyrroline *N*-oxide (DMPO, 97%) and 2,2,6,6-tetramethyl-piperidine (TEMP, 97%) were purchased from MACKLIN. Deionized water (DI water) was used throughout the process unless specified.

Synthesis of fluorinated cobalt oxyhydroxide

1.2 g of $Co(NO_3)_2 \cdot 6H_2O$, 0.8 g of $CO(NH_2)_2$, and 0.2 g of $NH_4 \cdot F$ were added to 100 mL of DI water and stirred for 30 min, then transferred to Teflon container at 140 °C for 2 h. After cooling to room temperature, the mixture was centrifuged to remove the transparent solution to obtain a solid catalyst (Co(OH)F, abbreviation: 1-FCO). 2-FCO and 3-FCO were prepared with the same hydrothermal conditions of 1-FCO. The 2-FCO was prepared using 2.4 g of $Co(NO_3)_2 \cdot 6H_2O$, 1.6 g of $CO(NH_2)_2$, and 0.4 g of $NH_4 \cdot F$, and 3-FCO was prepared using 3.6 g of $Co(NO_3)_2 \cdot 6H_2O$, 2.4 g of $CO(NH_2)_2$, and 0.6 g of $NH_4 \cdot F$.

Fabrication of 2-FCO/CAH

First, we added 1.0 g of sodium alginate and a certain 2-FCO to 100 mL DI water, stirred for 30 min, and subsequently placed in a water bath at 85 °C for 2 h to form a homogeneous solution. Then, $CaCl_2$ (0.1 g mL^{-1}) was added to the mixture. Afterward, the alginate hydrogel monolith spheres encapsulating fluorinated oxyhydroxide were prepared and named 2-FCO/CAH. The blank calcium alginate hydrogel (CAH) monolith spheres without 2-FCO were prepared using a similar procedure.

Characterizations

The microstructures of catalysts were characterized by scanning electron microscopy (SEM, ZEISS, Germany) and transmission electron microscopy (TEM, FEI TECNAI F20). The functional groups were detected by Fourier transform infrared

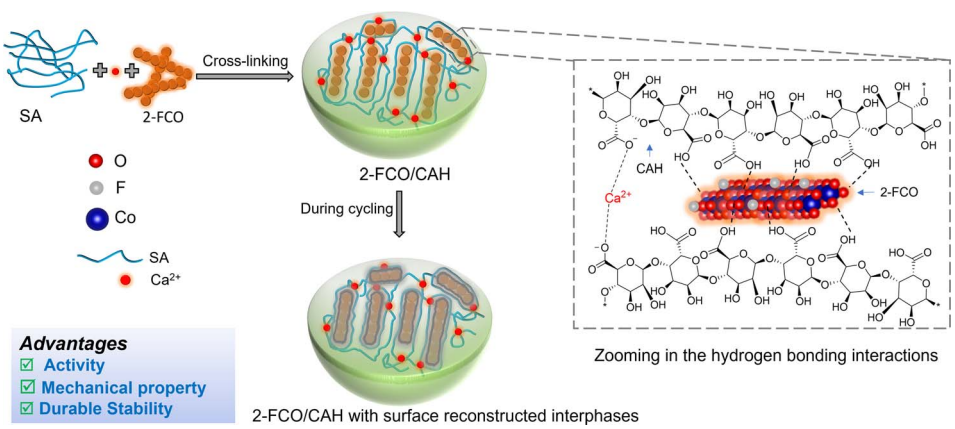

Scheme 1 Design principles of highly durable 2-FCO/CAH synthesis by collective hydrogen bonds and surface reconstructed interphase.

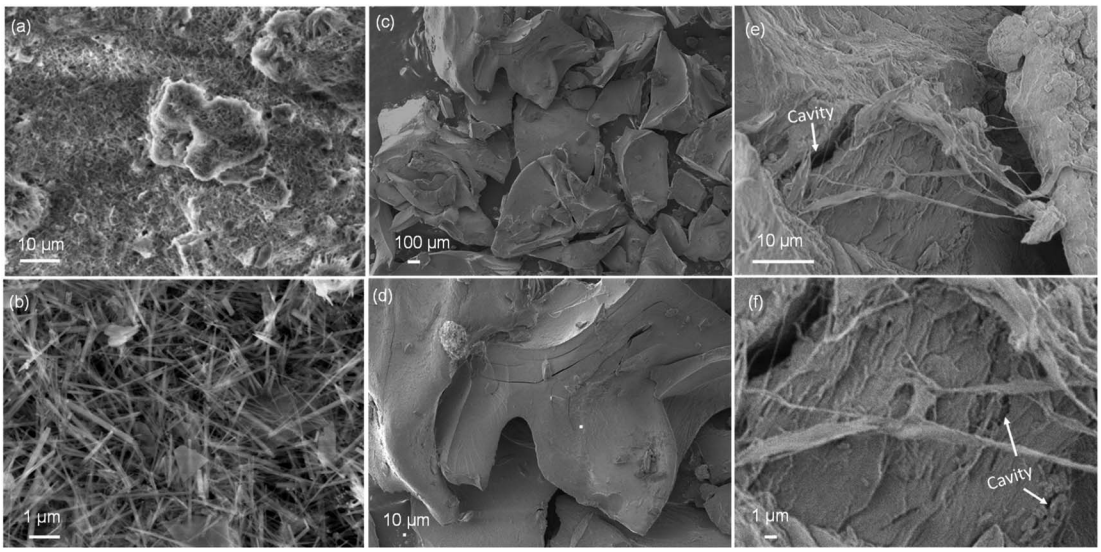

Fig. 1 SEM images of (a and b) 2-FCO, (c and d) CAH and (e and f) 2-FCO/CAH.

spectroscopy (FT-IR). The crystal phase was verified by X-ray powder diffraction spectrum (XRD, Rigaku, Japan) with Cu Kα radiation ($\lambda = 1.5406$ Å). The element content, distribution, and bonding energy were conducted by energy dispersed X-ray spectrum (EDS). At room temperature, the reactive species were detected based on electron spin resonance (ESR, Bruker). The degradation intermediates were characterized by high-performance liquid chromatograph-mass spectrum (HPLC-MS, Ultimate 3000 UHPLCQ Exactive, Thermo Scientific) with a mass spectrometer (Thermo Scientific Q Exactive) in a positive mode using a HESI source. The risk of intermediates was assessed by Toxicity Estimation Software Tool (T.E.S.T.5.1.1).

Degradation tests

The degradation tests involved a CIP solution (100 mL, 20 mg L^{-1}), PMS (2 mM), and FCO–CAH catalysts (equivalent to 20 mg of FCO) under room temperature. At first, FCO–CAH catalyst (equivalent to 20 mg of FCO) mixed with CIP solution (100 mL, 20 mg L^{-1}) and kept for 35 min to arrive in adsorption–desorption equilibrium. Next, high concentrated PMS was

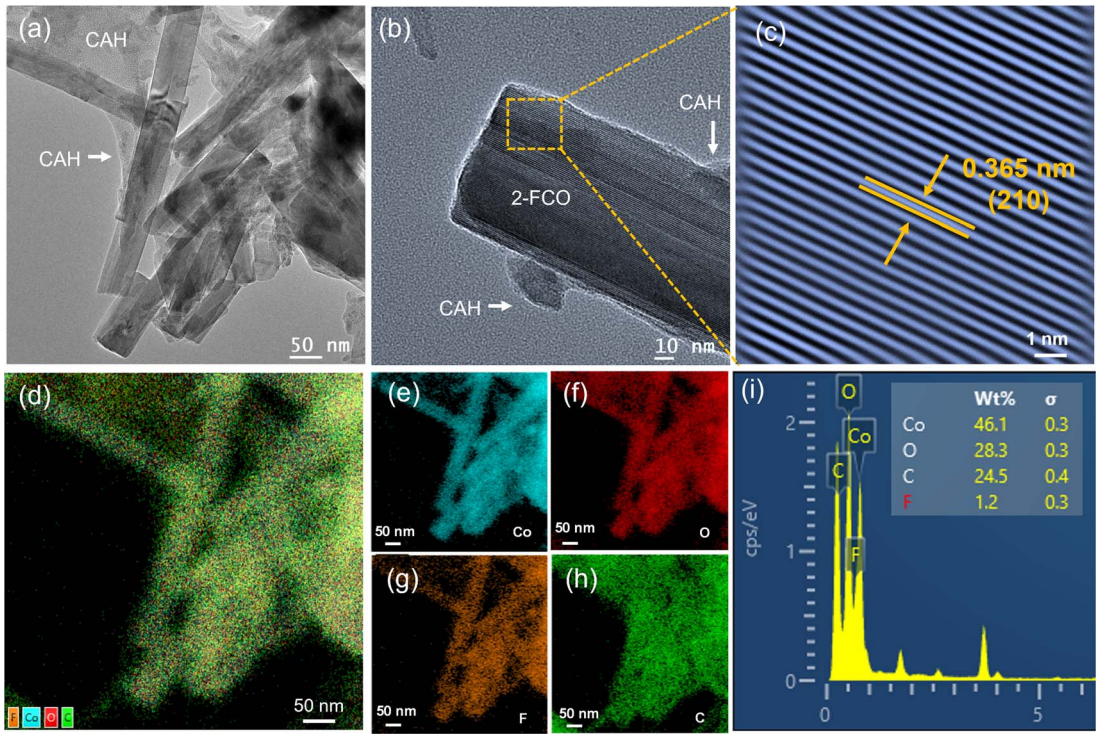

Fig. 2 (a and b) TEM image, (c) lattice spacing, (d–h) Co, O, F and C elemental mappings and (i) EDS (inset: element content) of 2-FCO/CAH.

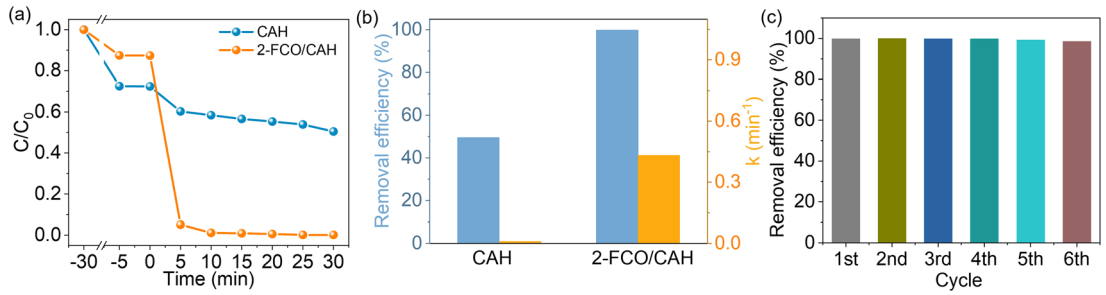

Fig. 3 (a) C/C_0 of CIP over time, (b) removal efficiency and first-order kinetic constant, and (c) cycling CIP degradation of 2-FCO/CAH (C_0 represents the initial concentration of CIP, not the abbreviation Co for cobalt).

added into FCO–CAH/CIP mixed solution and started timing simultaneously. At specific intervals, 1.0 mL of the mixture was withdrawn by a syringe and filtered *via* a 0.20 μm filter. For the catalyst durability test, the catalyst was reused after multiple washes with water. The concentrations of CIP throughout the experiment were analyzed using a high-performance liquid chromatograph equipped with a UV-vis detector (HPLC, Primaide, HITACHI).

Biological toxicity test

First, mung bean seeds are rinsed three times with deionized water and then soaked overnight in fresh deionized water. They are then divided into three portions and placed on pure cotton cloth, stored in the dark. They are watered with fresh TC solution, TC degradation solution, and deionized water, respectively, twice daily. The length of the mung bean sprouts is measured, and the total mass is weighed.

Discussion and result

Morphologies and chemical composition

The successful synthesis of 2-FCO/CAH was validated through XRD analysis, with the spectra (Fig. S1†) displaying the characteristic peaks of Co(OH)F (PDF# 50-0827) in both the 2-FCO and 2-FCO/CAH samples. The presence of CAH peaks within the 2-FCO/CAH XRD pattern corroborated the encapsulation of 2-

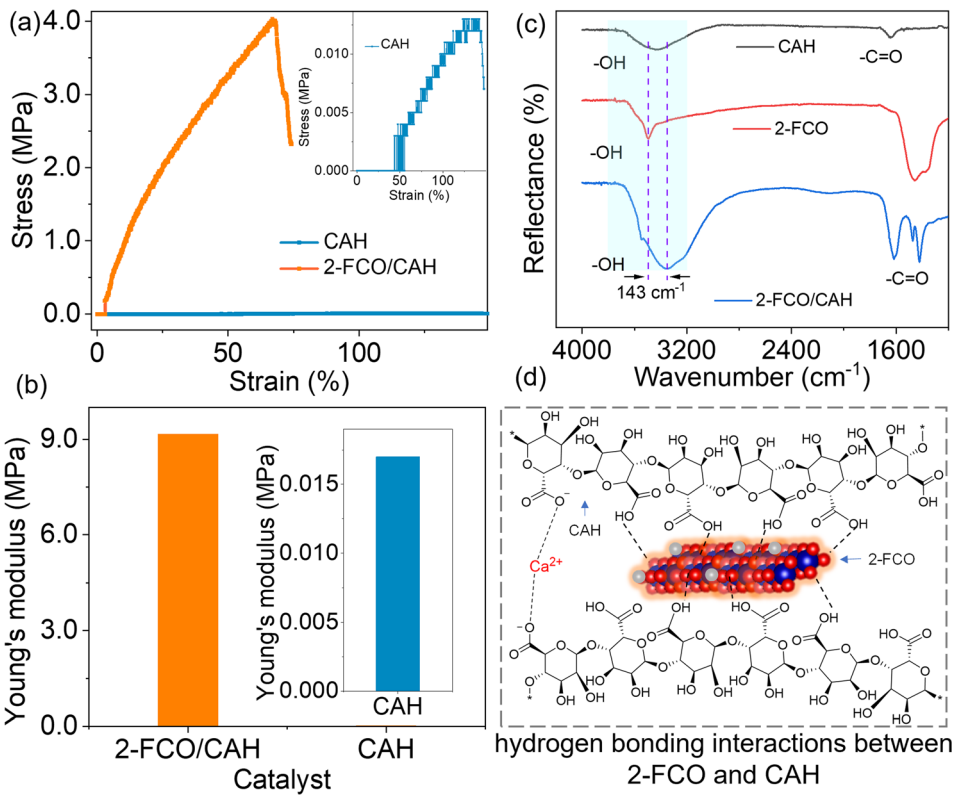

Fig. 4 (a) Mechanical tensile test of CAH and 2-FCO/CAH (inset: mechanical tensile test of CAH), (b) Young's modulus of CAH and 2-FCO/CAH, (c) FT-IR and (d) hydrogen bonding interaction between 2-FCO and CAH in 2-FCO/CAH catalyst.

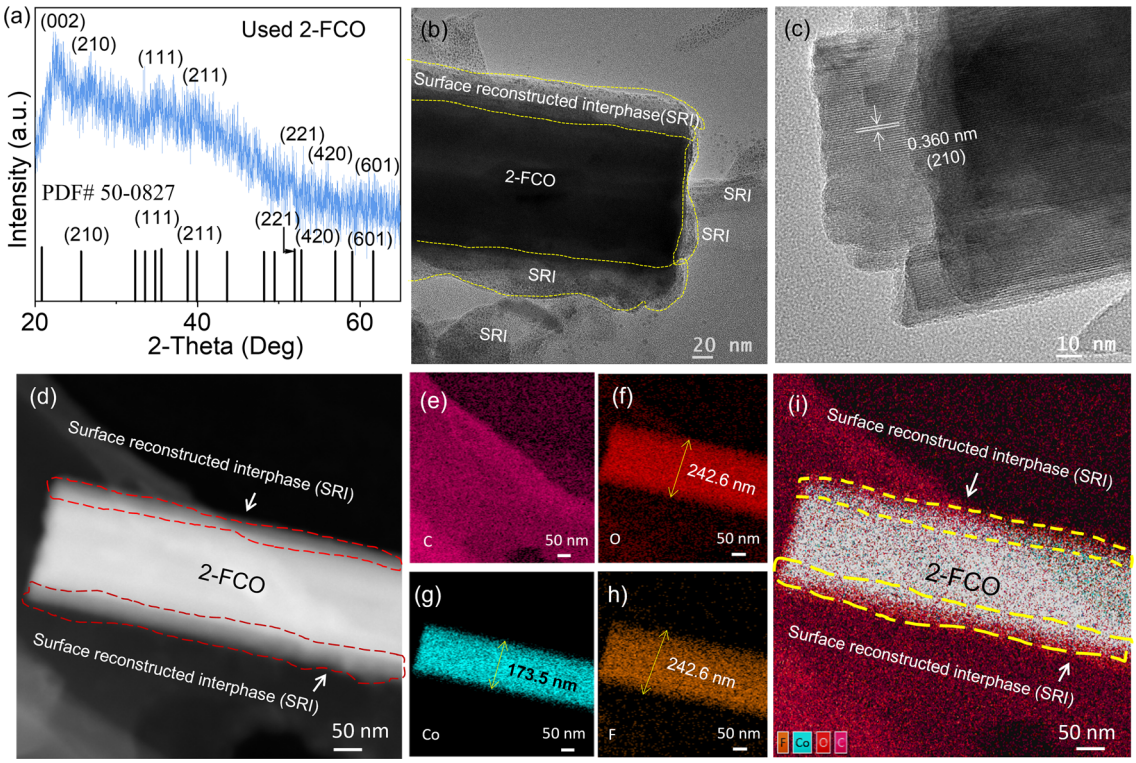

Fig. 5 (a) XRD pattern, (b and c) TEM images, (d) HAADF-STEM image and (e–i) elemental mappings of used 2-FCO/CAH after long-term cycling test.

FCO by the hydrogel matrix of CAH. Further SEM examinations revealed the morphological features of 2-FCO, CAH, and 2-FCO/CAH. The powdery 2-FCO consists of uniform, fiber-like structures with diameters consistently less than 0.2 μm (Fig. 1a and b). On the other hand, CAH appears as individual monoliths with a curved shape and a thickness of about 500 μm (Fig. 1c). SEM images at higher magnification (Fig. 1d) reveals a smooth surface on CAH, indicating its spherical structure with a smooth surface interface. In comparison, the multi-cavity structure consisting of hydrogen bond network can better enrich PMS and

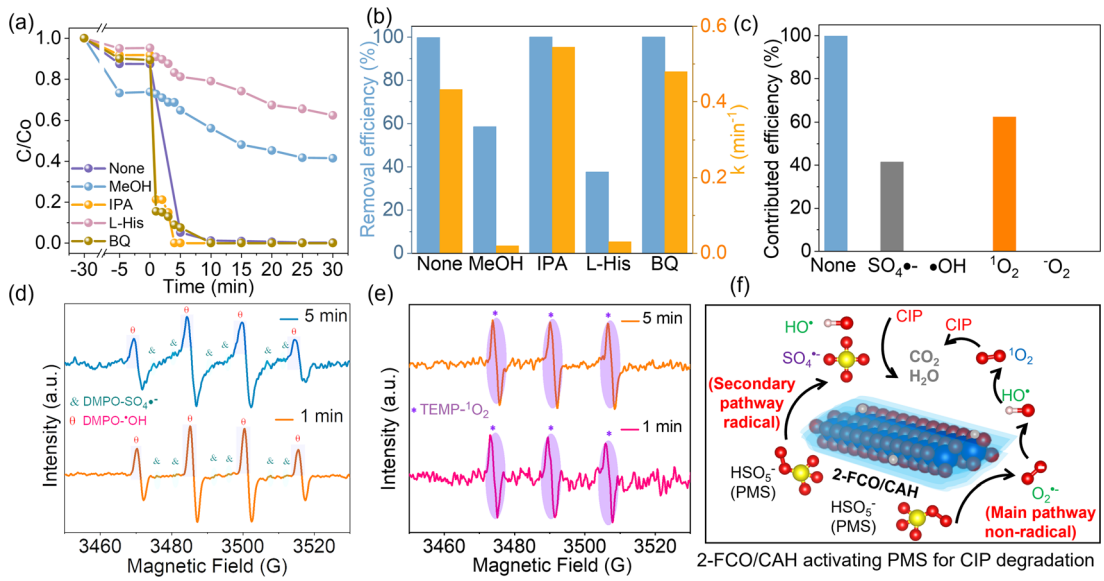

Fig. 6 Capturing test in the presence of various sacrificial agents: (a) CIP degradation, (b) removal efficiency and kinetic constants, (c) contribution efficiency of reactive species to CIP removal; EPR signals of (d) DMPO–·OH, DMPO–$SO_4^{\cdot-}$, (e) TEMP–$^1O_2$ and (f) CIP degradation mechanisms by 2-FCO/CAH/PMS.

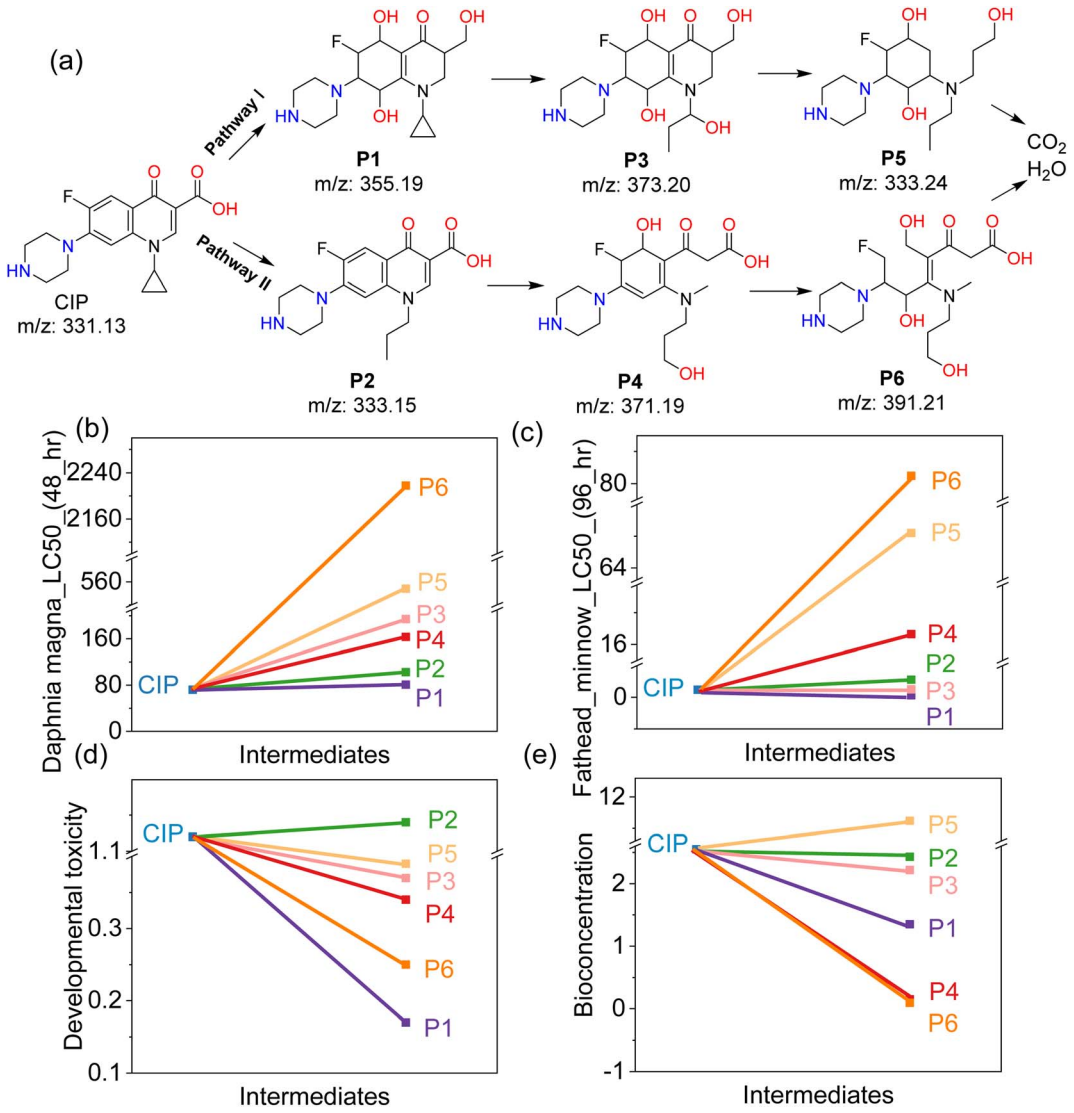

Fig. 7 (a) CIP degradation pathways and resulted intermediates by 2-FCO/CAH/PMS, (b) daphnia magna LC_50 (48_h), (c) fathead minnow LC_50 (96_h), (d) developmental toxicity and (e) bioconcentration of CIP and all resulted intermediates **P1–P6**.

antibiotics.[25] When 2-FCO is encapsulated by CAH (*i.e.*, 2-FCO/CAH), the interface becomes rough with an abundance of the cavity and shows a one-dimensional fiber structure (Fig. 1e), where the fiber-like 2-FCO is clearly embedded, creating a continuous connection with the hydrogel of CAH (Fig. 1f).

The detailed morphologies, composition and crystal plane structures were studied by TEM. Fig. 2a presents a uniform, one-dimensional fiber-like morphology of the 2-FCO–CAH with an average diameter of 100 nm. High-resolution TEM further provides detailed local structural information (Fig. 2b), revealing a regular fiber-like shape of 2-FCO and amorphous CAH adhering to the edges of the one-dimensional 2-FCO fibers. Furthermore, the lattice spacing of 2-FCO, denoted by the orange dashed rectangle in Fig. 2c, measures 0.365 nm, corresponding to the (210) plane of 2-FCO, which aligns with the XRD analysis. In addition to the lattice structures and shapes of 2-FCO–CAH, chemical compositions are worthy of being considerable. Elemental mapping images exhibit a consistent distribution of Co, O, F, and C elements within the 2-FCO/CAH (Fig. 2d–h). This elemental distribution is corroborated by energy-dispersive X-ray spectroscopy (EDS) mapping, verifying the 2-FCO/CAH composition (Fig. 2i).

PMS activation and catalyst durability

The PMS activation is intricately linked to the efficiency of CIP removal. Consequently, assessing CIP elimination rates can indicate the potential of catalysts to intensify the PMS activation. Fig. S2† shows that the 2-FCO had the highest activity. Thus, powdered 2-FCO was used for the upcoming study and discussion. Furthermore, Fig. 3a demonstrates that while CAH alone degrades CIP slowly in the presence of PMS, 2-FCO/CAH degrades CIP more rapidly than CAH alone due to 2-FCO/CAH with multi-cavity structure can enrich more PMS and CIP. The removal efficiency and kinetic constant of CIP is nearly 100%

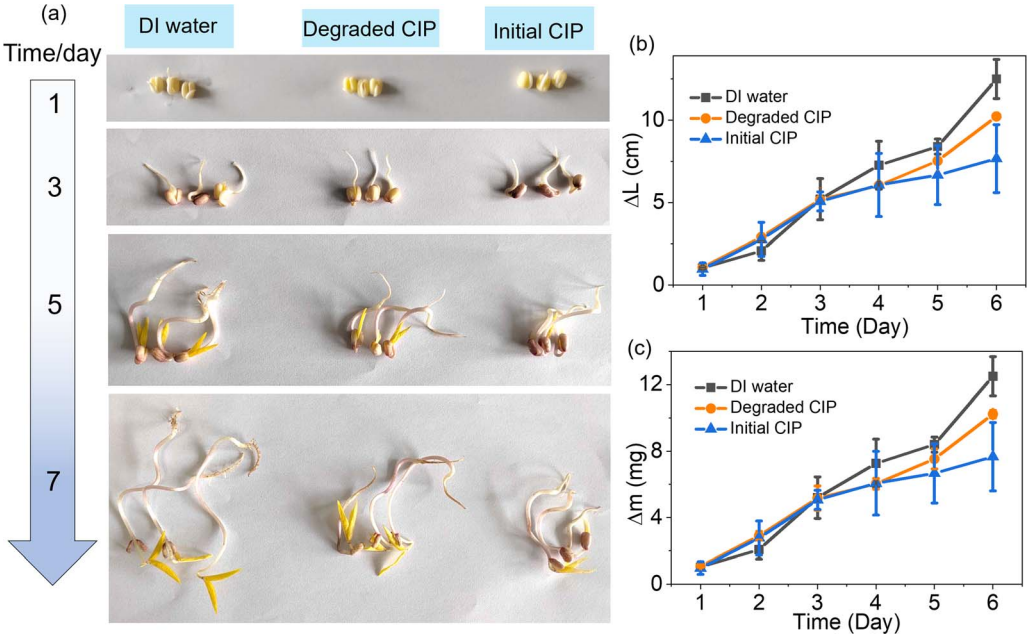

Fig. 8 (a) Photographs of mung bean sprout over time, (b) mung bean sprout growth length over time and (c) mung bean mass change over time across DI water, degraded CIP and initial CIP (20 mg L^{-1}).

and 0.433 min^{-1} for 2-FCO/CAH, significantly demonstrating the strengthening of PMS activation (Fig. 3b). Additionally, Fig. 3c shows that 2-FCO/CAH sustains robust activity over 6 consecutive cycles, maintaining a ~100% removal efficiency without decline. The degradation rate of CIP accelerates in long-term testing, suggesting that a self-optimizing phenomenon and robust mechanical property (we will discuss later) within the 2-FCO/CAH system improved its durability.

Mechanical property and interfacial stability

Mechanical tensile strength testing was employed to identify the mechanisms behind the enhanced performance of 2-FCO/CAH. Fig. 4a shows that the stress–strain curve of CAH gradually increases, reaching a maximum stress of 0.012 MPa at 141.5% strain (inset Fig. 4a). This indicates that pure CAH is highly compliant and susceptible to fracture, with relatively poor mechanical properties. In contrast, 2-FCO/CAH exhibits a significantly enhanced maximum stress of 4.02 MPa at 68.0% strain, marking a 335-fold increase over CAH. This enhancement suggests that the encapsulated 2-FCO significantly bolsters the tensile strength of CAH, indicative of the composite's robust mechanical properties and the inherent rigidity of the one-dimensional 2-FCO fibers. In addition, Young's modulus is a physical quantity describing the ability of a material to resist deformation within the elastic range. It is defined as the ratio of stress to strain when the material is under force, with the specific formula:

$$Y = \frac{\sigma}{\varepsilon} \quad (1)$$

Y is Young's modulus, σ is stress (the internal force per unit area), and ε is strain (the amount of deformation per unit length).

The Young's modulus of 2-FCO/CAH is 9.02 MPa, 531-fold larger than 0.017 MPa of CAH (Fig. 4b), implying an outstanding mechanical property of 2-FCO/CAH.

The mechanical tensile test also reveals a strong interaction between 2-FCO and CAH, as evidenced by a marked increase in tensile strength. To further probe this interaction, FT-IR analysis was conducted. In Fig. 4c, the –OH stretching vibrations (in the light blue region) at 3429 and 3503 cm^{-1} correspond to CAH and 2-FCO, respectively.[26,27] The encapsulation of 2-FCO within CAH leads to a noticeable broadening and downshift of the –OH peak in the FT-IR spectrum of 2-FCO/CAH, characterized by a wavenumber displacement of 143 cm^{-1}. The shifted –OH peak confirms the presence of robust collective hydrogen bonding interactions between CAH and its encapsulated 2-FCO along their interface.[26,28] Additionally, the –C=O peak at 1642 cm^{-1} in CAH shifts to 1620 cm^{-1} in the spectrum of 2-F-CoO/CAH (Fig. 4c), further supporting that the involved hydrogen bonds mainly form between –COOH of CAH and –OH of 2-FCO. We have provided a rational explanation for the hydrogen bonding mechanism between CAH and FCO at the molecular level, as depicted in Fig. 4d. Abundant hydrogen bonding between CAH polymer chains and 2-FCO fibers facilitates the even distribution of encapsulated 2-FCO, circumventing the aggregation typical of solid powders and enhancing the accessibility of catalytically active sites for PMS activation.[29–31] Consequently, beyond the intrinsic rigidity of the 2-FCO fibers, the robust collective hydrogen bonding interactions further enhance the 2-FCO/CAH composite's mechanical tensile properties, rendering them exceptional.

The robust mechanical properties of the 2-FCO/CAH catalyst underpin its sustained high efficiency in CIP removal, with mechanical stability vital to maintaining the catalyst's structural integrity. Understanding the structural and compositional evolution of 2-FCO/CAH is crucial for elucidating the

mechanism behind the cyclic durability. XRD analysis (Fig. 5a) on the used 2-FCO/CAH after six cycles revealed that the crystallographic planes, including (002), (210), (111), (211), (221), (420), and (601), remained consistent with the fresh 2-FCO/CAH and the standard PDF# 50-0827,[32] indicating a stable physiochemical property 2-FCO/CAH. TEM analyses further confirmed the retention of the one-dimensional fiber-like morphology of 2-FCO/CAH, with fibers approximately 100 nm in diameter (Fig. 5b). High-resolution TEM identified a ~40 nm thick solid surface interphase enveloping the 2-FCO fibers with (210) exposure (Fig. 5c), a feature not apparent in the fresh catalyst and attributed to the long-term recycling process. We refer to this generated interface as the surface reconstructed interphase, which likely correlates with the self-optimizing phenomenon of catalyst performance mentioned earlier. Similarly, high-angle annular dark-field scanning transmission electron microscopy (HAADF-STEM) has also well demonstrated the surface reconstructed interphase (indicated by the red dashed line frame) encapsulating 2-FCO (Fig. 5d). Moreover, the fiber-like image constructed by the elemental mapping of C, O, and F reaches a diameter of 242.6 nm (Fig. 5e–h), which is significantly larger than the elemental mapping image of Co (173.5 nm) (Fig. 5g). This indicates that the surface reconstructed interphase primarily comprises C, O, and F (Fig. 5i). This surface reconstructed interphase effectively sequesters leaching cobalt ions, mitigating the release of 2-FCO during cycling.

Interfering factors that affecting activity

In practical wastewater treatment, the activity of the 2-FCO/CAH is influenced by various factors such as pH, inorganic ions, and organic matter, which can modulate the activation of PMS. As depicted in Fig. S3a,† the CIP degradation efficiency under highly acidic conditions (pH 2.3) is not significantly different from that observed under neutral simulated conditions (pH 7.0). Conversely, at pH 11.7, the degradation process is impeded, suggesting that the 2-FCO/CAH catalyst is suboptimal for CIP removal under highly alkaline conditions (Fig. S3b†). Interestingly, chloride ions (Cl^-) significantly enhanced CIP degradation, indicating that these ions did not deactivate but promoted PMS activation (Fig. S3c†). However, the addition of carbonate (CO_3^{2-}) and bicarbonate (HCO_3^-) ions marginally inhibits CIP degradation, likely due to their reaction with sulfate and hydroxyl radicals to form secondary radicals (*i.e.*, $HCO_3^{\cdot}$ and $CO_3^{\cdot-}$) with lower oxidation potential (eqn (2)–(5)), which slightly dampen the degradation efficiency (Fig. S3d†).

$$HCO_3^- + SO_4^{\cdot-} \rightarrow HCO_3^{\cdot} + SO_4^{2-} \quad (2)$$

$$HCO_3^- + HO^{\cdot} \rightarrow HCO_3^{\cdot} + HO^- \quad (3)$$

$$CO_3^{2-} + SO_4^{\cdot-} \rightarrow CO_3^{\cdot-} + SO_4^{2-} \quad (4)$$

$$CO_3^{2-} + HO^{\cdot} \rightarrow CO_3^{\cdot-} + HO^- \quad (5)$$

Organic substances such as humic acid (HA) and bovine serum albumin (BSA) exhibit a negligible inhibitory effect, maintaining high degradation rates and removal efficiencies (Fig. S3e and f†). These findings indicate that the 2-FCO/CAH catalyst exhibits robust resistance to interference, demonstrating its potential for effective CIP degradation in complex aquatic environments.

PMS-activated mechanism and biological toxicity

The high removal efficiency of CIP is determined by the enhanced activation of PMS. Fig. 6 illustrates the degradation mechanisms of CIP by reactive species generated from the 2-FCO/CAH PMS system. Generally, the reactive species involved in CIP removal are transient, dissipating shortly after their production from PMS decomposition. To ascertain their roles, methanol (MeOH), L-histidine (L-His), benzoquinone (BQ), and isopropanol (IPA) were used as scavengers for $SO_4^{\cdot-}$, $^1O_2$, $O_2^{\cdot-}$ and $^{\cdot}OH$, respectively. As shown in Fig. 6a and b, a significant decrease in CIP concentration was observed after adding IPA or BQ to the system, with nearly complete removal within 10 minutes, suggesting that $O_2^{\cdot-}$ and $^{\cdot}OH$ play minor roles in CIP degradation. In contrast, adding MeOH results in a slower degradation rate, stabilizing at a 58.6% removal efficiency, whereas the presence of L-histidine leads to the slowest degradation but still achieves a high removal efficiency of 99.8%. Therefore, the $^1O_2$ is identified as the most influential reactive species, followed by $SO_4^{\cdot-}$, with $O_2^{\cdot-}$ and $^{\cdot}OH$ being the least significant (Fig. 6c). Compared to short-lived, easily interfered $^{\cdot}OH$ and $O_2^{\cdot-}$, long-lived, highly selective $^1O_2$ and $SO_4^{\cdot-}$ are more suitable for removing CIP.[33] The EPR signals of DMPO–$^{\cdot}$OH, DMPO–$SO_4^{\cdot-}$ and TEMP–$^1O_2$ are detected and increase over time (Fig. 6d and e), providing direct evidence of $SO_4^{\cdot-}$ and $^1O_2$ generation from 2-FCO/CAH PMS system. We combined these findings from scavenger experiments and EPR tests to create a diagram illustrating the reactive species involved in the CIP degradation process (Fig. 6f).

HPLC-MS analysis has delineated two principal pathways of CIP degradation by the 2-FCO/CAH PMS system, as outlined in Fig. 7a. For pathway I, the process starts with the dehydroxylation of CIP to form intermediate **P1** (*m*/*z* 355.19), which then undergoes propyl ring opening and hydroxylation to yield **P3** (*m*/*z* 373.20). Subsequently, further hexagonal ring cleavage and dehydroxylation produce **P5** (*m*/*z* 333.24), culminating in mineralization to CO_2 and H_2O. Alternatively, Pathway II CIP begins with the opening of CIP's cyclopropane ring to generate **P2** (*m*/*z* 333.15), followed by hydroxylation and ring opening to form **P4** (*m*/*z* 371.19) and **P6** (*m*/*z* 391.21), which also mineralizes to CO_2 and H_2O.

The possible risk of intermediate **P1–P6** is evaluated by Toxicity Estimation Software (T.E.S.T.5.1.1) based on the quantitative structure–activity relationship (QSAR) theory. Fig. 7b reveals that daphnia magna LC_50 of intermediates gradually increased from 8.66 mg L^{-1} (CIP) to 2240 mg L^{-1} (**P6**). Similarly, fathead minnow LC_50 of **P1–P6** increases from 0.48 mg L^{-1} (CIP) to 80.49 mg L^{-1} (**P6**) in Fig. 7c. The biological toxicity to daphnia magna and fathead minnow test verifies that the resulted intermediates have lower toxicities than CIP, reflecting the environmental benign of the 2-FCO/CAH PMS

system. Most intermediates show reduced developmental toxicity (Fig. 7d) and bioconcentration potential (Fig. 7e), highlighting that 2-FCO/CAH PMS has a universal environment-friendly nature.

To provide a clear and impactful demonstration of the effects of degradation products on biological growth and development, we utilize mung bean sprouts as a benchmark for toxicity assessment. We immersed mung bean seeds, previously soaked overnight, in three different solutions—DI water, degradation solution of CIP, and one with pristine CIP at a concentration of 20 mg L^{-1}—and monitored the sprouts' length (ΔL) and weight (Δm) throughout the study. The results in Fig. 8a show that the sprouts grown in the degraded CIP solution exhibited notably better growth than those in the initial CIP solution, approaching the sprouts grown in DI water. Fig. 8b adeptly quantifies the temporal changes in sprout growth, showing that the growth of sprouts across all three groups is nearly identical in the first 3 days. However, significant differences emerged after that, with the degraded CIP group's sprouts notably outperforming those of the initial CIP group in length. Consistent with the growth length trends, the fluctuations in the weight of the bean sprouts adhere to an analogous pattern (Fig. 8c). Taken together, these findings indicate that the biological toxicity of degraded CIP is significantly reduced compared to the initial CIP (20 mg L^{-1}), highlighting the environmental safety of the 2-FCO/CAH PMS system.

Conclusion

We developed a fluorinated cobalt oxyhydroxide (FCO) encapsulated within a calcium alginate hydrogel (FCO/CAH) *via* a straightforward physical mixing approach. The encapsulation ensures an even distribution of FCO, facilitated by hydrogen bonding with the hydrogel, which maximizes the exposure of active sites for PMS activation and thus enhances CIP degradation. The optimal formulation (*i.e.*, 2-FCO/CAH) shows a nearly 100% CIP removal efficiency. Notably, the long-term cyclic durability of 2-FCO/CAH is achieved by the enhanced mechanical properties and surface reconstructed interphase formed during cycling. The obtained 2-FCO/CAH can be used in a complex water environment and present a low toxicity and risk potential to the water environment. Our study also identifies the highly reactive species (*i.e.*, $^1O_2$ and $SO_4^{\bullet-}$) for enhanced PMS activation and proposes plausible degradation pathways for the CIP degradation process.

Data availability

Data will be made available on request.

Author contributions

Yunxiong Zeng: writing – review & editing, writing – original draft. Zhilong Zhang: investigation, formal analysis. Xingyu Zhan: data curation. Bo Hong: resources, data curation. Xinqing Wang: resources. Yingchun Xia: funding acquisition, data curation.

Conflicts of interest

The authors declare that they have no known competing financial interests or personal relationships that could have appeared to influence the work reported in this paper.

References

1 Y. Zeng, X. Zhan, B. Hong, Y. Xia, Y. Ding, T. Cai, K. Yin, X. Wang, L. Yang and S. Luo, Surface atom rearrangement on carbon nitride for enhanced photocatalysis degradation of antibiotics under visible light, *Chem. Eng. J.*, 2023, **452**, 139434.
2 H. Zhang, Y. Zeng, X. Wang, X. Zhan, J. Xu, A. Jin and B. Hong, Sea-Urchin carbon nitride with carbon vacancies (C-v) and oxygen substitution (O-s) for photodegradation of Tetracycline: Performance, mechanism insight and pathways, *Chem. Eng. J.*, 2022, **446**, 137053.
3 X. Zhan, Y. Zeng, J. Xu, Y. Xia, X. Wang, F. Tao, J. Ouyang, H. Li, L. Yang, S. Luo and B. Hong, Tailoring the three-phase microenvironment surface to induce carbon nitride oxide generating $\cdot O_2^-$ with 100% selectivity for ultrafast photodegradation tetracycline under visible light, *Chem. Eng. J.*, 2023, **464**, 142564.
4 A. C. Johnson, V. Keller, E. Dumont and J. P. Sumpter, Assessing the concentrations and risks of toxicity from the antibiotics ciprofloxacin, sulfamethoxazole, trimethoprim and erythromycin in European rivers, *Sci. Total Environ.*, 2015, **511**, 747–755.
5 L. Patrolecco, J. Rauseo, N. Ademollo, P. Grenni, M. Cardoni, C. Levantesi, M. L. Luprano and A. B. Caracciolo, Persistence of the antibiotic sulfamethoxazole in river water alone or in the co-presence of ciprofloxacin, *Sci. Total Environ.*, 2018, **640–641**, 1438–1446.
6 E. Turiel, G. Bordin and A. R. Rodríguez, Study of the evolution and degradation products of ciprofloxacin and oxolinic acid in river water samples by HPLC-UV/MS/MS-MS, *J. Environ. Monit.*, 2005, **7**, 189–195.
7 T. An, H. Yang, G. Li, W. Song, W. J. Cooper and X. Nie, Kinetics and mechanism of advanced oxidation processes (AOPs) in degradation of ciprofloxacin in water, *Appl. Catal., B*, 2010, **94**, 288–294.
8 M. Sayed, M. Ismail, S. Khan, S. Tabassum and H. M. Khan, Degradation of ciprofloxacin in water by advanced oxidation process: kinetics study, influencing parameters and degradation pathways, *Environ. Technol.*, 2016, **37**, 590–602.
9 M. Mahdi-Ahmed and S. Chiron, Ciprofloxacin oxidation by UV-C activated peroxymonosulfate in wastewater, *J. Hazard. Mater.*, 2014, **265**, 41–46.
10 W. Li, S. Li, Y. Tang, X. Yang, W. Zhang, X. Zhang, H. Chai and Y. Huang, Highly efficient activation of peroxymonosulfate by cobalt sulfide hollow nanospheres for fast ciprofloxacin degradation, *J. Hazard. Mater.*, 2020, **389**, 121856.
11 C. Fang, J. Yan, Y. Wang, N. Zhang and X. Liu, Facile synthesis of N-doped carbon nanorods for antibiotics degradation via PMS activation: Mechanism insight and

biotoxicity assessment, *Sep. Purif. Technol.*, 2024, **340**, 126849.

12 X. Zhang, W. Gu, D. Liu, L. Zhou, N. N. Huy, L. Wang, J. Zhang, Y. Liu and J. Lei, Fe(II) and pyridinic N complex sites synergy to activate PMS for specific generation of $^1O_2$ to degrade antibiotics with high efficiency, *Sci. Total Environ.*, 2023, **892**, 164067.

13 Y. H. Fan, Y. Q. Li, F. Hayat, C. Liu, J. Li and M. Chen, Multi-targeted removal of coexisted antibiotics in water by the synergies of radical and non-radical pathways in PMS activation, *Sep. Purif. Technol.*, 2023, **305**, 122475.

14 Y. Zeng, Z. Zhang, X. Zhan, J. Xu, S. Liu, F. Wu, J. Li, B. Hong, X. Wang and Y. Xia, The surface asymmetric site regulation of carbon nitride oxide enabling peroxymonosulfate activation for degrading tetracycline, *Sep. Purif. Technol.*, 2024, **344**, 127211.

15 X. Zhan, Z. Zhang, J. Xu, Z. Zhu, X. Wang, B. Hong, Y. Xia and Y. Zeng, Engineering commercial activated carbon with carbonyl site for activation of peroxymonosulfate and degradation of tetracycline, *Microchem. J.*, 2024, **200**, 110198.

16 Z. Zhang, X. Zhan, B. Hong, X. Wang, P. Tang, Y. Ding, Y. Xia and Y. Zeng, Edge interface microenvironment regulation of CoOOH/commercial activated carbon nano-hybrids enabling PMS activation for degrading ciprofloxacin, *J. Colloid Interface Sci.*, 2024, **663**, 909–918.

17 H. Xu, N. Jiang, D. Wang, L. Wang, Y. Song, Z. Chen, J. Ma and T. Zhang, Improving PMS oxidation of organic pollutants by single cobalt atom catalyst through hybrid radical and non-radical pathways, *Appl. Catal., B*, 2020, **263**, 118350.

18 X. Qiu, D. Ding, S. Yang, G. Wang, R. Chen, M. Dzakpasu, P. Jin and X. C. Wang, Solid-state synthesis of cobalt ferrite fitted with γ-Fe_2O_3-containing nanocage for peroxymonosulfate activation and cobalt leaching control, *Chem. Eng. J.*, 2021, **405**, 126994.

19 C. Zhu, Y. Yao, Q. Fang, S. Song, B. Chen and Y. Shen, Unveiling the Dynamic Evolution of Single-Atom Co Sites in Covalent Triazine Frameworks for Enhanced H_2O_2 Photosynthesis, *ACS Catal.*, 2024, **14**(5), 2847–2858.

20 Y. Wang, Y. Huang, G. Gou, N. Li, L. Li, Y. He, C. Liu, B. Lai and H. Sun, Dispersed cobalt embedded nitrogen-rich carbon framework activates peroxymonosulfate for carbamazepine degradation: cobalt leaching restriction and mechanism investigation, *Chemosphere*, 2023, **321**, 138026.

21 H. Ma, G. Wang, Z. Miao, X. Dong and X. Zhang, Integration of membrane filtration and peroxymonosulfate activation on CNT@nitrogen doped carbon/Al_2O_3 membrane for enhanced water treatment: Insight into the synergistic mechanism, *Sep. Purif. Technol.*, 2020, **252**, 117479.

22 T. Wang, W. M. de Vos and J. de Grooth, $CoFe_2O_4$-peroxymonosulfate based catalytic UF and NF polymeric membranes for naproxen removal: The role of residence time, *J. Membr. Sci.*, 2022, **646**, 120209.

23 J. Xue, J. Li, J. Gao, M. Wang and S. Ma, $CoFe_2O_4$ functionalized PVDF membrane for synchronous oil/water separation and peroxomonosulfate activation toward aromatic pollutants degradation, *Sep. Purif. Technol.*, 2022, **302**, 122120.

24 X. Zhan, Z. Zhang, J. Lin, J. Xu, X. Wang, B. Hong, Y. Xia and Y. Zeng, Surface atom rearrangement enabling graphitic carbon nitride/sodium alginate gel monolith for ultrafast completely photodegrading ciprofloxacin under visible light, *Chem. Eng. J.*, 2024, **489**, 151218.

25 Y. Duan, E. M. Pearce, T. K. Kwei, X. Hu, M. Rafailovich, J. Sokolov, K. Zhou and S. Schwarz, Surface Enrichment in Polymer Blends Involving Hydrogen Bonding, *Macromolecules*, 2001, **34**(19), 6761–6767.

26 S. R. Derkach, N. G. Voron'ko, N. I. Sokolan, D. S. Kolotova and Y. A. Kuchina, Interactions between gelatin and sodium alginate: UV and FTIR studies, *J. Dispersion Sci. Technol.*, 2020, **41**, 690–698.

27 G. Lozano-Vazquez, J. Alvarez-Ramirez, C. Lobato-Calleros, E. J. Vernon-Carter and N. Y. Hernández-Marín, Characterization of Corn Starch-Calcium Alginate Xerogels by Microscopy, Thermal, XRD, and FTIR Analyses, *Starch/Staerke*, 2021, **73**(7–8), 2000282.

28 R. Gautam, N. Kumar and J. G. Lynam, Theoretical and experimental study of choline chloride-carboxylic acid deep eutectic solvents and their hydrogen bonds, *J. Mol. Struct.*, 2020, **1222**, 28849.

29 Y. Ishida, L. Chabanne, M. Antonietti and M. Shalom, Morphology Control and Photocatalysis Enhancement by the One-Pot Synthesis of Carbon Nitride from Preorganized Hydrogen-Bonded Supramolecular Precursors, *Langmuir*, 2014, **30**, 447–451.

30 S. Dolai, S. K. Bhunia, P. Kluson, P. Stavarek and A. Pittermannova, Solvent-Assisted Synthesis of Supramolecular-Assembled Graphitic Carbon Nitride for Visible Light Induced Hydrogen Evolution – A Review, *ChemCatChem*, 2022, **14**, e202101299.

31 F. M. Raymo, M. D. Bartberger, K. N. Houk and J. F. Stoddart, The Magnitude of [C–H···O] Hydrogen Bonding in Molecular and Supramolecular Assemblies, *J. Am. Chem. Soc.*, 2001, **123**, 9264–9267.

32 S. Guo, Y. Wu, C. Wang, Y. Gao, M. Li, B. Zhang and C. Liu, Electrocatalytic hydrogenation of quinolines with water over a fluorine-modified cobalt catalyst, *Nat. Commun.*, 2022, **13**, 5297.

33 Z.-H. Xie, C.-S. He, D.-N. Pei, Y. Dong, S.-R. Yang, Z. Xiong, P. Zhou, Z.-C. Pan, G. Yao and B. Lai, Review of characteristics, generation pathways and detection methods of singlet oxygen generated in advanced oxidation processes (AOPs), *Chem. Eng. J.*, 2023, **468**, 143778.